Subseasonal Variability of U.S. Coastal Sea Level from MJO and ENSO Teleconnection Interference

Marybeth C. Arcodia[a b] Emily Becker,[c] Ben P. Kirtman[a c]

[a] *University of Miami Rosenstiel School of Marine, Atmospheric, and Earth Science, Miami FL*

[b] *Colorado State University, Fort Collins CO* [c] *Cooperative Institute for Marine and Atmospheric Science, Miami FL*

Corresponding author: Marybeth C. Arcodia, marcodia@earth.miami.edu

ABSTRACT: Climate variability affects sea levels as certain climate modes can accelerate or decelerate the rising sea level trend, but subseasonal variability of coastal sea levels is under-explored. This study is the first to investigate how remote tropical forcing from the MJO and ENSO impact subseasonal U.S. coastal sea level variability. Here, composite analyses using tide gauge data from six coastal regions along the East and West Coasts of the U.S. reveal influences on sea level anomalies from both the MJO and ENSO. Tropical MJO deep convection forces a signal that results in U.S. coastal sea levels anomalies that vary based on MJO phase. Further, ENSO is shown to modulate both the MJO sea level response and background state of the teleconnections. The sea level anomalies can be significantly enhanced or weakened by the MJO-associated anomaly along the East Coast due to constructive or destructive interference with the ENSO-associated anomaly, respectively. The West Coast anomaly is found to be dominated by ENSO. Consistent relationships between low-level zonal and meridional winds and sea level pressure are found to be spatially-varying drivers of the variability. Two case studies reveal how MJO and ENSO teleconnection interference played a role in notable coastal flooding events. Much of the focus on sea level rise concerns the long-term trend associated with anthropogenic warming, but on shorter time scales, we find subseasonal climate variability has the potential to exacerbate the regional coastal flooding impacts.

Significance Statement

Coastal flooding due to sea level rise is increasingly threatening communities, but natural fluctuations of coastal sea levels can exacerbate the human-caused sea level rise trend. This study assesses the role of tropical influences on coastal subseasonal (2 week - 3 month) sea level heights. Further, we explore the mechanisms responsible, particularly for constructive interference of signals contributing to coastal flooding events. Subseasonal signals amplify the lower frequency signals, resulting in increased or decreased sea level heights than those expected from known climate modes (e.g. ENSO). Low-level onshore winds and reduced sea level pressure connected to the tropical phenomena are shown to be indicators of increased U.S. coastal sea levels, and vice versa. Two case studies reveal how MJO and ENSO teleconnection interference played a role in notable coastal flooding events. Much of the focus on sea level rise concerns the long-term trend associated with anthropogenic warming, but on shorter time scales, we find subseasonal climate variability has the potential to exacerbate the regional coastal flooding impacts.

1. Introduction

Sea level rise is a hazard to coastal communities in a continuously warming climate, with many coastal and island communities already feeling the impacts of sea level rise (Church and White 2011). Impacts include increased damage from storm surge (Dasgupta et al. 2009), economic disruption from high-tide flooding (Hino et al. 2019), and threatened low-lying infrastructure (Martello and Whittle 2023; Buchanan et al. 2020). While anthropogenic climate change has led to global sea level rise primarily via thermal expansion and land-ice melt, many areas, especially along the East Coast of the United States, are experiencing more rapid sea level rise than the global average (Sweet et al. 2017). The Intergovernmental Panel of Climate Change Sixth Assessment Report (IPCC 2022) recently reported that anthropogenic drivers will continue to increase the exposure and vulnerability of coastal communities to future sea level rise without major adaptation efforts compared to today. Therefore, much of the focus on future sea level rise and increased flood exposure risk across sectors is on sea level hazards due to anthropogenic warming (Swain et al. 2020; Warren-Myers and Hurlimann 2022; Griggs 2021; Nicholls et al. 2021).

As flooding becomes increasingly threatening to coastal communities, it is crucial to understand how internal variability can modulate and temporarily enhance or suppress the underlying sea level rise trend. Further, recent findings by Li et al. (2022) show that due to sea level rise, exceedance of high tide flooding events occurs more frequently, but typically daily tidal anomaly fluctuations are insufficient for flooding threshold exceedance alone. These findings highlight the importance of investigating non-tidal sea level variability, since increased sea level anomalies from sea level variability ultimately exacerbate coastal impacts, particularly coastal flooding (Long et al. 2021). A primary climate mode affecting sea levels is the El Niño Southern Oscillation (ENSO) which operates on seasonal to interannual timescales (Hamlington et al. 2015). Major coastal flooding and high tide along the U.S. East and West Coasts have higher probabilities linked to El Niño (Andrews et al. 2004; Menéndez and Woodworth 2010; Sweet and Park 2014; Muis et al. 2018). Sweet and Zervas (2011) showed that during El Niño winter months, there is higher average sea level along the Mid-Atlantic Coast than during Neutral or La Niña conditions due to changes in regional sea level pressure. Further, during El Niños, coastal winter storm tracks and prevailing winds increase the average number of extratropical winter storms impacting the East Coast, leading to higher sea levels (Hirsch et al. 2001; Sweet and Zervas 2011; Thompson et al. 2013). On the U.S. West Coast, El Niños are similarly linked to positive sea level anomalies and negative sea level anomalies during La Niñas during boreal winter months (Barnard et al. 2015) due to both remotely forced and coastally trapped (e.g. Kelvin) waves (Ryan and Noble 2002).

While ENSO dominates coastal sea levels on seasonal to interannual timescales, sea level variability is influenced by competing climate modes on varying timescales. Sweet et al. (2018) outline known factors which impact sea level and their temporal scales and respective potential sea level magnitude changes on daily, seasonal, and interannual scales. On longer timescales, multi-year tidal cycles (predominantly a 4.4-year and 18.6-year cycle) can contribute to extreme high water events (Merrifield et al. 2013; Enríquez et al. 2022), and decadal to centennial variability has also been detected in sea level extremes (Marcos et al. 2015; Marcos and Woodworth 2017).

Lacking from these analyses is a focus on the subseasonal (2 week through 3 months) timescale. Often called the ”desert of predictability” (Vitart et al. 2017), subseasonal prediction of extremes can mitigate human loss of life and financial devastation from disasters (Vitart et al. 2019). Increased subseasonal predictability can result from leveraging known climate modes of variability and identifying predictable states of the climate system (Mariotti et al. 2020). Here, we focus on two predominant climate modes of tropical variability, the Madden-Julian Oscillation (MJO) and the El Niño Southern Oscillation (ENSO), both known to produce global tropical-extratropical teleconnection patterns (Zhang 2013; Roundy 2012; Diaz et al. 2001; Stan et al. 2017). Upper level divergent flow associated with the deep tropical convection of the MJO and ENSO excites poleward-propagating stationary Rossby waves which produce an extratropical response (Hoskins and Karoly 1981; Held and Kang 1987). The MJO, the dominant mode of tropical subseasonal variability, is an eastward propagating phenomenon characterized by coupling between mid-level condensational heating and tropospheric circulation (Madden and Julian 1971, 1972; Zhang 2005). The MJO produces Northern Hemisphere wintertime teleconnection responses via atmospheric blocking, temperature, and precipitation changes (Henderson et al. 2016; Jenney et al. 2019; Becker et al. 2011) with response patterns varying based on MJO phase (e.g. spatial pattern, sign of anomaly) (Tseng et al. 2019). The El Niño Southern Oscillation (ENSO), the dominant mode of interannual tropical variability, produces well-documented tropical-extratropical Northern Hemisphere teleconnection responses (Diaz et al. 2001; Alexander et al. 2002; Yeh et al. 2018; Taschetto et al. 2020), and is known to have an imprint on subseasonal variability (Compo et al. 2001; Chapman et al. 2021).

The MJO and low frequency modulation by ENSO has been shown to influence subseasonal circulation and precipitation patterns in the North Pacific and subsequently the United States (Moon et al. 2011; Henderson et al. 2017; Tseng et al. 2020). For example, Arcodia et al. (2020) found subseasonal MJO signals and interannual ENSO signals can constructively and destructively interfere to produce rainfall anomalies throughout the United States. During particular phases of the active MJO, the study found the associated signal can enhance or overwhelm the precipitation signal that is expected from ENSO, as was found when the MJO and ENSO positive precipitation signals constructively interfered and contributed to the extreme flooding event in the Mississippi river basin region in December of 2015.

However, limited previous research has been conducted on how coastal sea levels have been influenced by the Madden-Julian Oscillation and the background ENSO state. Oliver and Thompson (2010) found that MJO-related onshore winds resulted in sea level changes in Australia and Matthews et al. (2004) found a similar relationship in Antarctica, but the MJO influence on the East and West Coasts of the United States remains unexplored.

Here, we build upon the analysis of Arcodia et al. (2020) to examine the combined effects of the MJO and ENSO on U.S. subseasonal coastal sea levels and offer new insight into subseasonal prediction of coastal sea level variability. We diagnose possible mechanisms through which the tropical MJO convection affects U.S. coastal sea levels and how these factors, including low-level winds and sea level pressure, vary by region. We conclude with a summary and a discussion on the significance of understanding subseasonal variability and remote influences on U.S. coastal sea levels and potential flooding impacts.

2. Data and Methods

The data used to assess coastal water levels are the non-tidal residual (NTR) at six U.S. coastal tide gauge stations: Virginia Key (Miami), FL; Key West, FL; Sewell's Point (Norfolk), VA; Charleston, SC; Annapolis, MD; and San Francisco, CA. Each of these cities is densely populated and highly vulnerable to current and future coastal flooding (Sweet et al. 2018). The NTR value is the sea level not related to the tides or the seasonal cycle and only that related to anomalous water levels, storm surge, and wave setup (Sweet et al. 2015). In short, the NTR is the component of the sea level with the astronomical tidal element removed. The water level data used for calculating the non-tidal residual is available from the Center for Operational Oceanographic Products and Services (CO-OPS) (http://tidesandcurrents.noaa.gov/). The data used are hourly values from 1996-2017. The maximum NTR value is taken for each day to create a daily NTR timeseries for each tide gauge station. The daily data are then de-trended to remove any trend from sea level rise. The daily anomaly is calculated by removing the daily climatology.

MJO phases are calculated by the authors using the Real-time Multivariate MJO Index (Wheeler and Hendon 2004) using NCEP-NCAR Reanalysis-2 data (Kalnay et al. 1996). Following the methodology of Arcodia et al. (2020), the daily anomalies are calculated by removing the daily climatology. Similar analyses were performed to calculate daily anomalies by removing the daily climatology and the first three harmonics, however, results were virtually indistinguishable. To obtain the MJO-associated daily anomaly, a centered 120-day running mean of the daily anomalies is subtracted to remove the effect of ENSO (Lin et al. 2008) without retaining unwanted interannual variability (Arcodia et al. 2020; Ren et al. 2022) found when using the previous 120-day running mean as in Wheeler and Hendon (2004). Days are categorized into eight active and one inactive

MJO phases during November-April as boreal winter has the strongest MJO teleconnections in the Northern Hemisphere (Zhang 2005). Only days in which the MJO Index amplitude exceeded 1 standard deviation (e.g. active MJO days) were included. Phases correspond to the location of the deep convection associated with the MJO as it propagates from the tropical Indian Ocean, over the Maritime Continent and to the Western and Central Pacific. MJO phases are combined to increase sample size, such that MJO phases 2&3 are referred to as P23, phases 4&5 are referred to as P45, and so on for P67 and P81.

El Niño (warm) and La Niña (cold) ENSO periods are defined by the NOAA Climate Prediction Center (CPC): exceeding a threshold of ±0.5°C for the oceanic Niño index (ONI), a 3-month running mean of ERSST.v5 SST anomalies in the Niño-3.4 region (5°N–5°S, 120°–170°W), based on centered 30-yr base periods updated every 5 years. Composites are made using two simultaneous conditions: MJO phase and ENSO phase. The ENSO-associated anomaly is the centered 120-day running mean of the daily anomaly that was subtracted from the MJO-associated anomaly. The MJO+ENSO anomaly is the summation of the two anomalies, i.e. the daily anomaly.

NCEP-NCAR Reanalysis 2 data (Kalnay et al. 1996) are used to diagnose the mechanism for the teleconnection patterns. We use 850 hPa zonal and meridional wind, sea surface temperature, and sea level pressure daily data at 2.5^o resolution from 1996-2017 for consistency with the NTR timeseries data. The seasonal cycle and ENSO-related signals are removed in the same way as the NTR data. The use of the NCEP-NCAR Reanalysis dataset for calculating the MJO Index and documenting associated teleconnection patterns is justified by Arcodia et al. (2020) who calculate the MJO Index in the same way and assess related teleconnection patterns and found comparable anomaly patterns in the reanalysis and observational datasets.

Composites for the 850 hPa zonal wind, sea level pressure, and sea surface temperature are calculated in the same way as the NTR (Figs. 3-5) but shown as maps instead of bar charts due to the 3-dimensional structure of the anomalies. Statistical significance for each analysis is described in the Results section.

3. Results

a. MJO-ENSO Interference of NTR Anomalies

We analyze how MJO teleconnections can affect the persistent signals associated with the ENSO teleconnections to determine if the MJO can notably affect the overall anomaly signal. We analyze each signal individually and combined to determine if and where the ENSO and MJO signals constructively or destructively interfere to produce U.S. coastal NTR anomalies. The time-averaged constructive and destructive interference from the NTR dataset is shown in Figures 1 and 2.

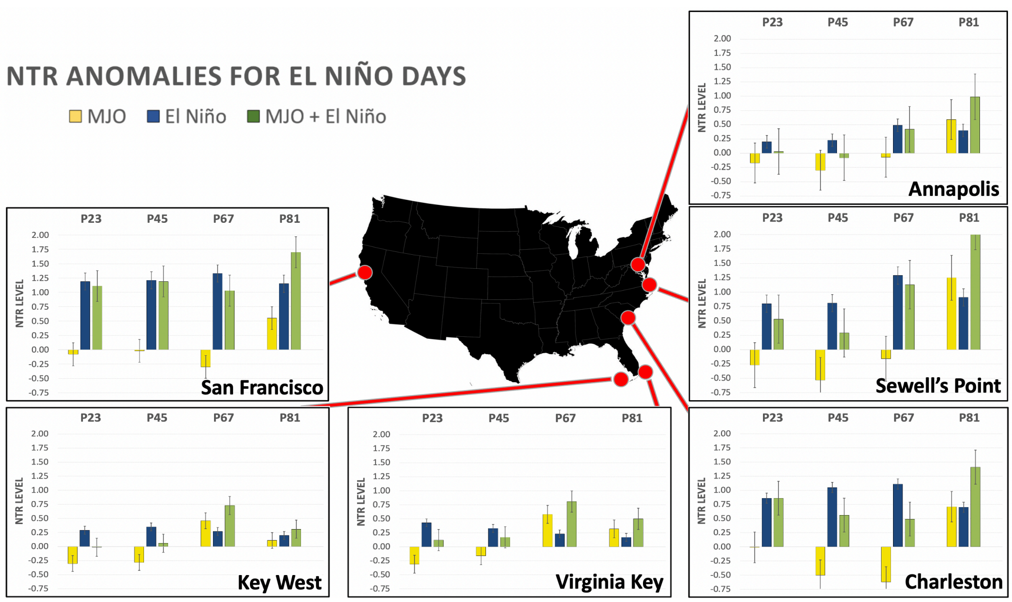

FIG. 1. The Non-Tidal Residual (NTR) anomalies in millimeters from six tide gauges (San Francisco, Charleston, Key West, Virginia Key, Sewell's Point, and Annapolis) broken down by MJO phase (P23, P45, P67, P81) from 1996 to 2017 for active MJO days in November–April during all El Niño (positive ENSO) days . The yellow bars show MJO-only anomalies, the blue bars show the ENSO-only anomalies, and the green bars are the MJO+ENSO anomalies. The error bars show plus/minus one standard deviation of 10,000 bootstrapped samples.

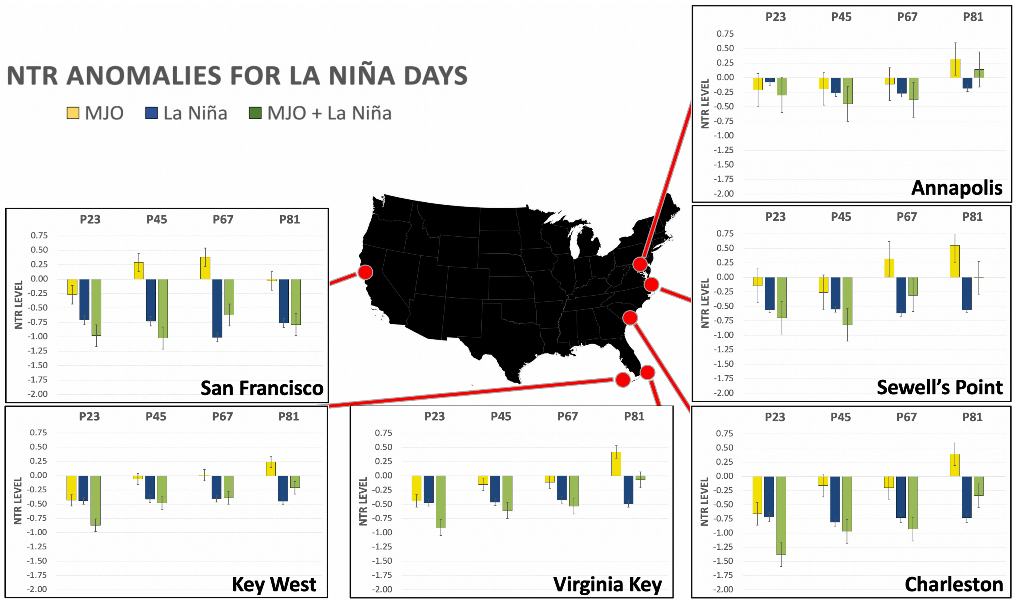

FIG. 2. The Non-Tidal Residual (NTR) anomalies in millimeters from six tide gauges (San Francisco, Charleston, Key West, Virginia Key, Sewell's Point, and Annapolis) broken down by MJO phase (P23, P45, P67, P81) from 1996 to 2017 for active MJO days in November–April during all La Niña (negative ENSO) days . The yellow bars show MJO-only anomalies, the blue bars show the ENSO-only anomalies, and the green bars are the MJO+ENSO anomalies. The error bars show plus/minus one standard deviation of 10,000 bootstrapped samples.

2

Composites of the NTR are calculated for every day from 1996 to 2017 during El Niño events then further broken down by MJO phase in Fig. 1 for El Niño days and Fig. 2 for La Niña days. In Fig. 1, boxes correspond to the six U.S. tide gauges used in this study with 4 panels for each MJO phase pair (P23, P45, P67, P81) with 3 bars each. The yellow bars (MJO-only) are the composites of the MJO-forced anomaly of all days between November and April from 1996 to 2017 when there was an El Niño event ongoing and the MJO was active and in the indicated phases. The blue bar represents the NTR from the same days in which a simultaneous there was an El Niño event and the MJO was the indicated phases; however, it is an average of only the interannual anomaly associated with El Niño based on the centered 120-day mean of the data. The green bars represent the same days composited for the adjacent yellow and green bars, but summing the MJO and ENSO anomalies. Thus, the green bars represent the total NTR anomaly averaged over all days when the MJO was active and in the indicated phases during an El Niño event from November to April during 1996–2017. Days in which either an El Niño or a La Niña event *and* a concurrent active MJO occurred comprise approximately 40% of all boreal winter days in the data used.

Tables 1 and 2 are the numeric values of the NTR anomalies in millimeters broken down by MJO and ENSO phases corresponding to the bar charts in Fig. 1 and Fig. 2, respectively. To compute statistical significance, we use the bootstrapping resampling technique, a statistical method in which data is randomly resampled with replacement (Tibshirani and Efron 1993). We bootstrapped 10,000 samples for each MJO-ENSO phase combination (e.g. values comprising each bar chart were bootstrapped 10,000 times), subsampling 80% of the samples in each, then computed the standard deviation of the bootstrapped values. One positive and one negative standard deviation of the bootstrapped samples are shown in the error bars in Figs. 1 and 2. The numeric values of the bootstrapped standard deviations are shown in Tables 1 and 2. MJO phases in which constructive interference between the MJO and ENSO associated anomalies occurred are bolded. The rightmost column for each tide gauge station shows the percentage of the combined MJO + ENSO anomaly relative to the total anomaly standard deviation. This is a measure of significance of impact for how much the MJO-associated, ENSO-associated, or combined anomalies contribute to the overall anomaly on a given day.

San Francisco

MJO Phase	MJO	El Niño	MJO+ El Niño	Percent of Total Anom Stdv
P23	-0.08 ± 0.16	1.19 ± 0.12	1.11 ± 0.22	0.44 ± 0.09
P45	-0.02 ± 0.24	1.21 ± 0.17	1.19 ± 0.27	0.47 ± 0.11
P67	-0.30 ± 0.15	1.33 ± 0.17	1.03 ± 0.21	0.41 ± 0.08
P81	**0.55 ± 0.25**	**1.15 ± 0.14**	**1.7 ± 0.32**	**0.67 ± 0.13**

Charleston

MJO Phase	MJO	El Niño	MJO+ El Niño	Percent of Total Anom Stdv
P23	-0.01 ± 0.22	0.86 ± 0.09	0.86 ± 0.23	0.23 ± 0.06
P45	-0.50 ± 0.27	1.05 ± 0.09	0.56 ± 0.27	0.15 ± 0.07
P67	-0.62 ± 0.29	1.11 ± 0.09	0.49 ± 0.32	0.13 ± 0.08
P81	**0.71 ± 0.29**	**0.70 ± 0.09**	**1.41 ± 0.33**	**0.37 ± 0.09**

Annapolis

MJO Phase	MJO	El Niño	MJO+ El Niño	Percent of Total Anom Stdv
P23	-0.17 ± 0.30	0.2 ± 0.10	0.03 ± 0.31	0.01 ± 0.07
P45	-0.30 ± 0.41	0.23 ± 0.12	-0.08 ± 0.43	0.02 ± 0.10
P67	-0.07 ± 0.37	0.49 ± 0.14	0.42 ± 0.38	0.10 ± 0.09
P81	**0.59 ± 0.40**	**0.40 ± 0.11**	**0.99 ± 0.43**	**0.24 ± 0.10**

Key West

MJO Phase	MJO	El Niño	MJO+ El Niño	Percent of Total Anom Stdv
P23	-0.30 ± 0.10	0.29 ± 0.07	-0.01 ± 0.13	0.01 ± 0.07
P45	-0.28 ± 0.14	0.35 ± 0.09	0.06 ± 0.17	0.03 ± 0.09
P67	**0.46 ± 0.14**	**0.27 ± 0.07**	**0.73 ± 0.16**	**0.40 ± 0.09**
P81	**0.11 ± 0.15**	**0.20 ± 0.07**	**0.31 ± 0.17**	**0.17 ± 0.09**

Virginia Key

MJO Phase	MJO	El Niño	MJO+ El Niño	Percent of Total Anom Stdv
P23	-0.31 ± 0.10	0.43 ± 0.07	0.12 ± 0.12	0.06 ± 0.06
P45	-0.16 ± 0.18	0.33 ± 0.09	0.17 ± 0.19	0.08 ± 0.09
P67	**0.58 ± 0.16**	**0.23 ± 0.06**	**0.81 ± 0.19**	**0.37 ± 0.09**
P81	**0.32 ± 0.18**	**0.17 ± 0.06**	**0.50 ± 0.20**	**0.23 ± 0.09**

Sewell's Point

MJO Phase	MJO	El Niño	MJO+ El Niño	Percent of Total Anom Stdv
P23	-0.27 ± 0.37	0.80 ± 0.12	0.53 ± 0.39	0.11 ± 0.08
P45	-0.53 ± 0.39	0.81 ± 0.17	0.29 ± 0.42	0.06 ± 0.09
P67	-0.16 ± 0.39	1.29 ± 0.17	1.13 ± 0.40	0.24 ± 0.09
P81	**1.25 ± 0.47**	**0.91 ± 0.14**	**2.16 ± 0.53**	**0.46 ± 0.11**

TABLE 1. NTR anomaly numeric value broken down by MJO and ENSO phase in millimeters corresponding to the bar charts in Fig. 1 for each of the six U.S. tide gauge stations analyzed. The rightmost column of each table shows the percentage of the combined MJO+El Niño anomaly to the total anomaly standard deviation. Values include plus/minus one standard deviation computed via 10,000 iterations of bootstrapping. MJO phases in which constructive interference occurred are bolded.

1

San Francisco

MJO Phase	MJO	La Niña	MJO+ La Niña	Percent of Total Anom Stdv
P23	**-0.27 ± 0.16**	**-0.71 ± 0.08**	**-0.98 ± 0.19**	**0.39 ± 0.07**
P45	0.29 ± 0.15	-0.73 ± 0.09	-0.45 ± 0.20	0.18 ± 0.08
P67	0.38 ± 0.12	-1.01 ± 0.08	-0.62 ± 0.16	0.24 ± 0.06
P81	**-0.03 ± 0.17**	**-0.76 ± 0.10**	**-0.79 ± 0.20**	**0.31 ± 0.08**

Charleston

MJO Phase	MJO	La Niña	MJO+ La Niña	Percent of Total Anom Stdv
P23	**-0.66 ± 0.20**	**-0.72 ± 0.08**	**-1.38 ± 0.21**	**0.36 ± 0.05**
P45	**-0.16 ± 0.20**	**-0.81 ± 0.07**	**-0.97 ± 0.21**	**0.25 ± 0.05**
P67	**-0.20 ± 0.19**	**-0.73 ± 0.07**	**-0.93 ± 0.21**	**0.24 ± 0.05**
P81	0.39 ± 0.26	-0.73 ± 0.09	-0.34 ± 0.28	0.09 ± 0.07

Annapolis

MJO Phase	MJO	La Niña	MJO+ La Niña	Percent of Total Anom Stdv
P23	**-0.21 ± 0.31**	**-0.08 ± 0.06**	**-0.30 ± 0.33**	**0.07 ± 0.08**
P45	**-0.19 ± 0.26**	**-0.26 ± 0.07**	**-0.45 ± 0.28**	**0.11 ± 0.07**
P67	**-0.11 ± 0.26**	**-0.27 ± 0.06**	**-0.38 ± 0.26**	**0.09 ± 0.06**
P81	0.32 ± 0.35	-0.18 ± 0.07	0.14 ± 0.35	0.03 ± 0.08

Key West

MJO Phase	MJO	La Niña	MJO+ La Niña	Percent of Total Anom Stdv
P23	**-0.43 ± 0.09**	**-0.44 ± 0.06**	**-0.87 ± 0.11**	**0.47 ± 0.06**
P45	**-0.06 ± 0.09**	**-0.41 ± 0.06**	**-0.48 ± 0.11**	**0.26 ± 0.06**
P67	0.01 ± 0.10	-0.40 ± 0.06	-0.39 ± 0.11	0.21 ± 0.06
P81	0.24 ± 0.13	-0.45 ± 0.07	-0.21 ± 0.17	0.11 ± 0.09

Virginia Key

MJO Phase	MJO	La Niña	MJO+ La Niña	Percent of Total Anom Stdv
P23	**-0.44 ± 0.10**	**-0.47 ± 0.06**	**-0.91 ± 0.12**	**0.42 ± 0.06**
P45	**-0.15 ± 0.11**	**-0.46 ± 0.06**	**-0.61 ± 0.12**	**0.28 ± 0.06**
P67	**-0.11 ± 0.11**	**-0.42 ± 0.06**	**-0.53 ± 0.13**	**0.24 ± 0.06**
P81	0.42 ± 0.14	-0.49 ± 0.07	-0.07 ± 0.18	0.03 ± 0.08

Sewell's Point

MJO Phase	MJO	La Niña	MJO+ La Niña	Percent of Total Anom Stdv
P23	**-0.14 ± 0.26**	**-0.56 ±0.05**	**-0.70 ± 0.26**	**0.15 ± 0.06**
P45	**-0.26 ± 0.29**	**-0.55 ± 0.04**	**-0.82 ± 0.30**	**0.18 ± 0.06**
P67	0.32 ± 0.25	-0.62 ± 0.05	-0.31 ± 0.25	0.07 ± 0.05
P81	0.55 ± 0.35	-0.56 ± 0.05	-0.01 ± 0.35	0.00 ± 0.07

TABLE 2. NTR anomaly numeric value broken down by MJO and ENSO phase in millimeters corresponding to the bar charts in Fig. 2 for each of the six U.S. tide gauge stations analyzed. The rightmost column of each table shows the percentage of the combined MJO+La Niña anomaly to the total anomaly standard deviation. Values include plus/minus one standard deviation computed via 10,000 iterations of bootstrapping. MJO phases in which constructive interference occurred are bolded.

2

It is important to note that while the interannual variability has been removed via subtraction of the 120-day centered running mean, ENSO modulates the background state through which the MJO is propagating and the MJO itself and can thus modify the MJO-associated teleconnections. Thus, the interannual signal and subseasonal signal are separated, but they are not necessarily linearly independent. Further, each MJO phase corresponds to approximately 5-10 days per phase (Yadav and Straus 2017; Zheng and Chang 2019), and each panel contains a combination of 2 phases, or 10-20 days days. Extratropical circulation anomalies are observed as a response to a tropical heating forcing approximately 10-20 days later, with an average of two weeks needed for the stationary Rossby wave to fully develop (Matthews et al. 2004). Therefore, consideration of a lag between the MJO forcing and the extratropical response is not needed for the composite analyses.

The five East Coast tide gauge stations have similar signals from ENSO (e.g. a positive anomaly during El Niño events and a negative anomaly during La Niña events) with variations in the magnitude, while the MJO signals vary by location.

The Virginia Key tide gauge station is located on the East Coast of the U.S. in Miami, Florida. In Virginia Key, the persistent ENSO signals are a positive NTR anomaly during El Niños and a negative NTR anomaly during La Niñas (Figs. 1, 2). However, during MJO P23 and P45, the MJO-associated NTR anomalies are negative during both El Niños and La Niñas. This leads to destructive interference between the MJO and ENSO signals during El Niños and constructive interference during La Niñas, reducing and enhancing the daily NTR anomalies, respectively. In P67 and P81 during El Niños, the MJO and ENSO signals constructively interfere and enhance the ENSO signal, while in P81 during La Niñas, the MJO and ENSO signals destructively interfere, almost cancelling the signal altogether (Tables 1, 2). During P23 and P45, the MJO anomaly during El Niños and La Niñas is negative, and during P81 the MJO anomaly during both ENSO phases is positive. However, during P67, the MJO anomaly is positive during El Niños but negative during La Niñas. This difference of the sign of the MJO anomaly during different ENSO states highlights the modulation of the MJO-signal by the ENSO base state, consistent with previous literature showing modulation of the MJO teleconnection by MJO (Tseng et al. 2020; Moon et al. 2011; Arcodia and Kirtman 2023).

The Key West, Florida tide gauge follows a similar pattern to Virginia Key, which is not surprising due to the close proximity of the two tide gauge stations (Figs. 1, 2). However, of note during P23 during El Niños, the MJO and ENSO signals destructively interfere, and the magnitude of the MJO signal is approximately equal to that of the ENSO signal, resulting in a near-zero NTR anomaly during those MJO phases (Tables 1, 1).

The Sewell's Point tide gauge station is located in Norfolk, Virginia. At Sewell's Point, the ENSO signals are similar to those in Virginia Key and Key West in that the ENSO-associated anomaly is positive during El Niños and negative during La Niñas, consistent with the findings of Sweet et al. (2018) (Figs. 1, 2). During El Niños, there is destructive interference between the MJO and ENSO signals in P23 and P45, but there is constructive interference in P23 and P45 during La Niñas. The opposite occurs in P81 when there is constructive interference during El Niños, resulting in a combined anomaly over 2x the magnitude due to ENSO alone. This constructive interference accounts for nearly 50% of the total anomaly standard deviation (Table 1). Conversely, destructive interference during La Niñas which nearly cancels the signal and results in a near-zero NTR anomaly (Table 2), highlighting the importance of considering the MJO-associated anomaly in addition to the ENSO-association anomaly. Similar to Virginia Key, the sign of the MJO-associated NTR anomaly during P67 is opposite during El Niños and La Niñas due to modulation by the ENSO base state. The magnitudes of the Sewell's Point combined NTR anomalies are roughly double those of Virginia Key and Key West during La Niñas and triple those during El Niños, indicating that Sewell's Point has a strong influence from both the MJO and ENSO. These larger sea level anomalies are likely due to Sewell's Point location on the mid-East Coast, which generally results in higher seas and potential exacerbation of sea levels due to short-term internal variability related to the North Atlantic Oscillation and Gulf Stream transport changes (Ezer and Atkinson 2014; Ezer 2019), but further investigation into these additional influences from climate modes of variability is needed.

The Charleston, South Carolina tide gauge follows a similar trend to the Sewell's Point tide gauge. During El Niños and P45 and P67, the MJO signal destructively interferes with the ENSO signal, weakening the NTR anomaly, but during P81, the MJO and ENSO signals constructively interfere resulting in an increased NTR anomaly of roughly double the magnitude from the MJO and ENSO anomalies individually. The constructive interference results in approximately 37% of the total anomaly standard deviation (Table 1). During La Niñas, there is a similar relationship but during P23 in which the MJO and ENSO signals constructively interfere to produce a decreased sea level anomaly accounting for roughly 36% of the total anomaly standard deviation (Table 2).

The Annapolis, Maryland tide gauge station differs from the other East Coast tide gauges discussed in that it is located on the Chesapeake Bay, inland from the coast, but has still experienced frequent flooding (Hino et al. 2019; Sweet et al. 2019). During P23 and P45, the MJO and ENSO signals destructively interfere during El Niños, resulting in near-zero NTR anomalies, but constructively interfere during La Niñas resulting in strong negative NTR anomalies. Conversely, in P81, the MJO and ENSO signals constructively interfere during El Niños, resulting in an approximate doubling of the ENSO-associated anomaly and roughly 24% of the total anomaly standard deviation. During La Niñas, the signals destructively interfere resulting in a near-zero positive anomaly, despite the persistent negative anomaly associated with La Niña (Tables 1, 2), highlighting events where the MJO-associated anomaly can overwhelm the expected ENSO signal.

On the West Coast of the U.S., the San Francisco, California tide gauge station experiences the same ENSO effect as the East Coast in that during El Niños, the NTR is higher on average than during La Niñas, consistent with the findings of Sweet et al. (2018); Andrews et al. (2004); Goodman et al. (2018). However, unlike the East Coast cities, in San Francisco, the ENSO signal dominates the overall NTR anomaly. During El Niños and La Niñas, the MJO-associated anomaly can act to constructively or destructively interfere with the ENSO-associated anomaly, but it is small relative to the ENSO-associated anomaly and only slightly enhances or weakens the ENSO signal (Tables 1, 2). This relationship between ENSO and San Francisco sea level anomalies is likely due to coastally trapped Kelvin waves propagating along the West Coast of the U.S. as a direct response to ENSO forcing (Ryan and Noble 2002; Barnard et al. 2015), This results in San Francisco sea levels being linked more to ENSO than the MJO, while the East Coast has comparable sea level anomaly contributions from both MJO and ENSO signals.

Filtering of the daily NTR anomalies at six U.S. coastal tide gauge locations reveals that the MJO can significantly enhance or mask the ENSO signals on the East Coast of the U.S. during particular phases of the MJO, but the West Coast NTR anomalies are dominated by the ENSO signal. It is important to note that constructive interference of the MJO and ENSO signals can lead to significant contributions to the overall anomaly, such as in San Francisco for all MJO phases during El Niño events, Sewell's Point during an MJO P81 during El Niño events, and Key West during P23 during La Niña events. Further, destructive interference can cancel the MJO and ENSO signals such as in Key West during P23 during El Niños and in Virginia Key during P81 during La Niñas.

b. Possible Mechanism Diagnosis of Coastal Sea Level Anomalies

Composites of 850 hPa zonal wind (Fig. 3), sea level pressure (SLP; Fig. 4), and sea surface temperature (SST; Fig. 5) are calculated for the MJO-only anomalies, ENSO-only anomalies, and MJO+ENSO anomalies (i.e. the daily anomaly) broken down by MJO and ENSO phase for November through April from 1996-2017. Anomalies which exceed two standard deviations of the daily variable computed over the number of independent samples within composites are stippled to identify significance.

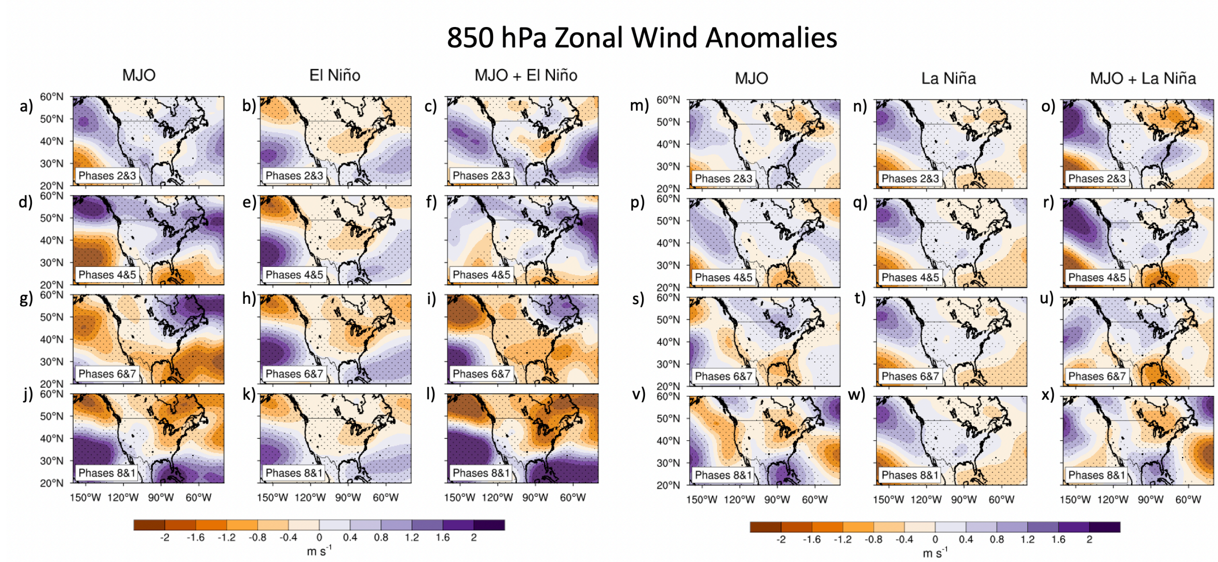

FIG. 3. 850 hPa zonal wind anomalies (m s^{-1}) broken down by MJO phase from 1996 to 2017 for active MJO days in November–April during (left) all El Niño (positive ENSO) days and (right) all La Niña (negative ENSO) days. MJO P23 are in the top row, followed by P45, P67, and P81 in the bottom row. Stippling indicates anomalies which exceed two standard deviations.

The MJO-associated anomaly varies with both MJO and ENSO phase. Fluctuations in the anomaly patterns between MJO phases reveal that the MJO deep convection does have a subseasonal teleconnection response in the 850 hPa zonal wind and sea level pressure anomalous patterns over North America. Furthermore, differences between the MJO anomalies during El Niño (Fig. 3-4a,d,g,j) and La Niña (Fig. 3-4m,p,s,v) suggest that the ENSO background state is modulating the MJO teleconnection response.

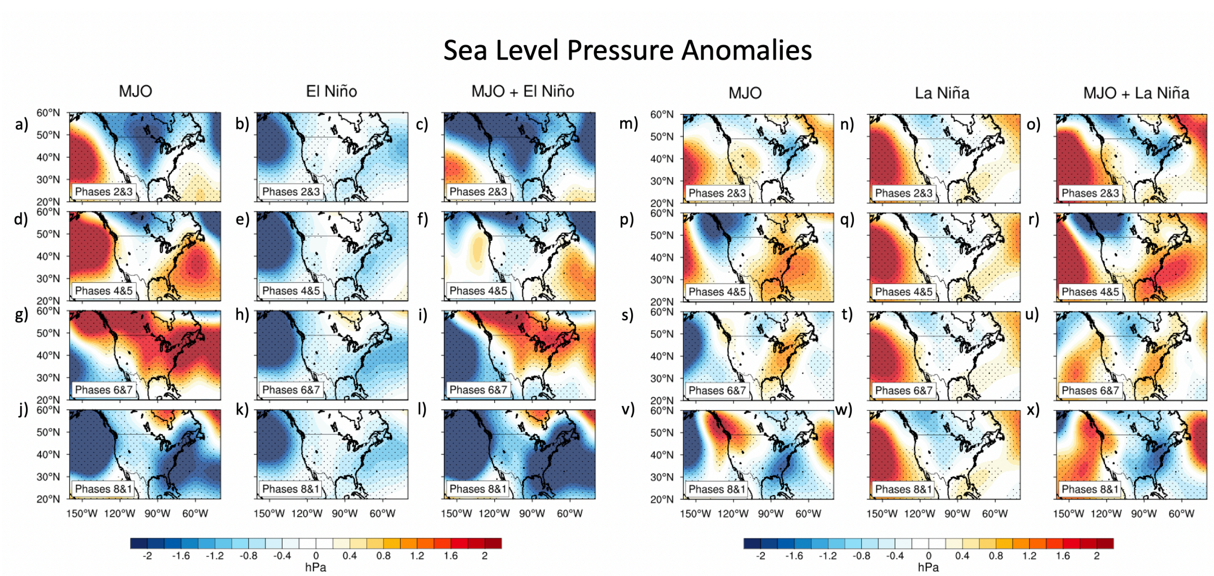

FIG. 4. Sea level pressure anomalies (mb) broken down by MJO phase from 1996 to 2017 for active MJO days in November–April during (left) all El Niño (positive ENSO) days and (right) all La Niña (negative ENSO) days. MJO P23 are in the top row, followed by P45, P67, and P81 in the bottom row. Stippling indicates anomalies which exceed two standard deviations.

The zonal winds in MJO P23 and P81 over Florida are westerly anomalies which constructively interfere with the El Niño signal (Fig. 3a-c,j-l) and weaken the mean easterly flow, but destructively interfere with the La Niña signal (Fig. 3m-o,v-x), masking the La Niña wind anomaly, and vice versa for P45 and P67. However, these wind patterns are not reflective of the NTR anomalies found at the tide gauge stations in Virginia Key, FL and Key West, FL (Figs. 1, 2). The SLP anomalies (Fig. 4) show negative pressure anomalies persistent for El Niño and positive pressure anomalies for La Niña along the East and West Coasts. The MJO-associated anomaly destructively interferes with the negative El Niño anomaly in P45 and P67 (Fig. 4d-i), weakening the SLP anomaly near Florida, but constructively interferes in P81 (Fig. 4j-l), leading to a strong negative anomaly. The negative SLP causes a doming effect and higher water levels which is reflected in the NTR levels in Virginia Key and Key West during P81 El Niño days (Fig. 1). Additionally, during La Niña days, constructive interference from the positive MJO-associated anomaly in P45, and destructive interference with the negative anomaly in P81 are also reflected in the Virginia Key and Key West tide gauges (Fig. 2). These results suggest that SLP anomalies are a better indicator of coastal NTR anomalies in Florida than low-level zonal winds anomalies.

At the Mid-Atlantic/Southern East Coast tide gauges analyzed, Sewell's Point and Charleston, the zonal wind anomalies associated with the MJO destructively interfere with the El Niño easterlies in P45 (Fig. 3d-f) and constructively interfere in P81 (Fig. 3j-l), leading to anomalous onshore winds, and this is reflected in the Sewell's Point and Charleston NTR anomalies (Fig. 1). The SLP anomalies in these regions follow a similar pattern, with destructive interference in P45 and constructive interference in P81 during El Niños. During La Niñas, both the 850 hPa zonal wind and SLP anomalies are of weaker magnitude. Opposite to the El Niño-day patterns, there is constructive interference in P45 and destructive interference in P81 during La Niñas which is also reflected in the Sewell's Point and Charleston NTR anomalies (Fig. 2). Therefore, both the low-level zonal winds and the SLP are good indicators of coastal NTR anomalies at Sewell's Point and Charleston, with stronger signals during El Niños than La Niñas. The Annapolis, MD 850 hPa zonal winds and SLP anomalies follow a similar tendency for MJO-associated and ENSO-associated anomalies to the East Coast tide gauge stations. We note that the location of the Annapolis tide gauge on the Chesapeake Bay relatively farther inland than the other stations suggests that there could potentially be additional factors (e.g., runoff) affecting the water levels that are beyond the scope of this study.

On the West Coast during El Niños in P45 (Fig. 3d-f), the MJO-associated anomaly is a strong easterly off the coast of California which destructively interferes with the ENSO-associated westerly, nearly cancelling the ENSO signal in California. The opposite occurs during P81(Fig. 3j-l), in which the MJO-associated anomaly in the same region is westerly, constructively interfering with the ENSO signal and resulting in strong westerly flow. However, Figures 1 and 2 shows that the NTR anomalies in San Francisco are dominated by the ENSO signal. The SSTs along the California coast (see Fig. 5) are also dominated by the ENSO signal over the MJO signal, supporting the argument that the NTR in the West Coast is a direct response to ENSO (consistent with Andrews et al. (2004)) with little influence from the MJO.

The SSTs were analyzed to determine if SST anomalies could impact sea levels via thermal expansion and contraction. The composite analysis for SST anomalies (Fig. 5) reveals that the MJO-associated anomaly does have a signal along the East and West Coasts, with stronger signals during El Niños than La Niñas. Along the West Coast, the MJO-associated anomaly destructively interferes with the ENSO-associated anomaly in P45 (Fig. 5d-f, p-r) and constructively interferes in P81 (Fig. 5j-l, v-x), and vice versa for the East Coast. These interference patterns are not consistent with the NTR anomalies found at the East Coast tide gauge locations, suggesting that SST anomalies are not a good indicator of coastal water levels along the East Coast.

Similarly to the NTR anomaly composites in Figs. 1-2, the variable field composite maps show that the MJO-associated anomalies vary between MJO phases (e.g. on subseasonal timescales) as well as based on ENSO phase. While the ENSO-associated anomalies do not vary significantly on subseasonal timescales, the constructive and destructive interference between the MJO and ENSO anomalies can play a role in modulating the NTR anomaly observed on the coast.

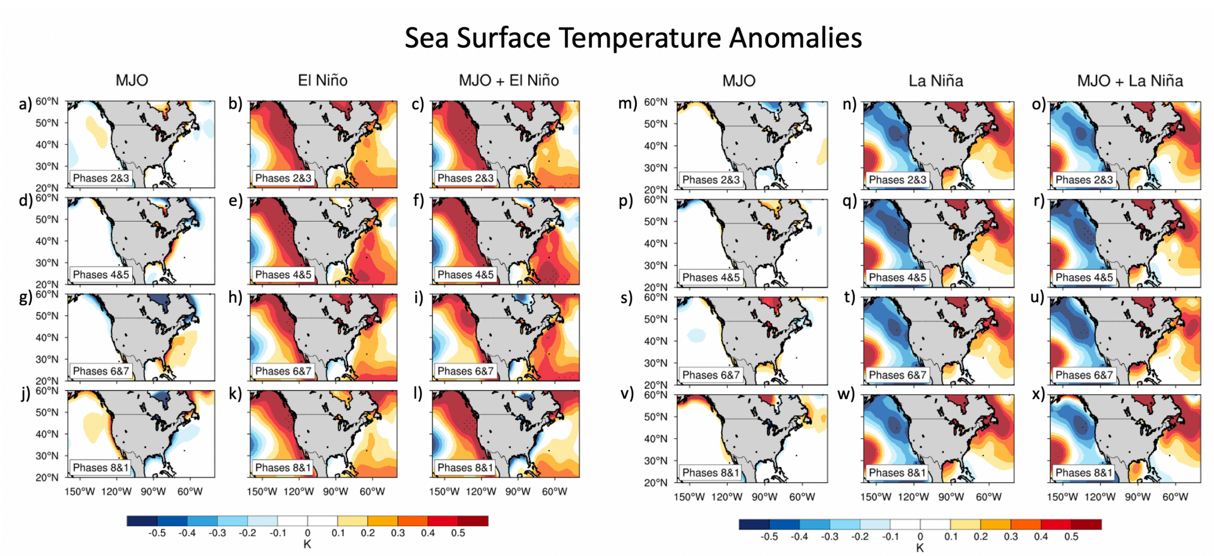

FIG. 5. Sea surface temperature anomalies (Kelvin) broken down by MJO phase from 1996 to 2017 for active MJO days in November–April during (left) all El Niño (positive ENSO) days and (right) all La Niña (negative ENSO) days. MJO P23 are in the top row, followed by P45, P67, and P81 in the bottom row. Stippling indicates anomalies which exceed two standard deviations.

5

Figures 3-5 show instances of both constructive and destructive interference that varies temporally, based on MJO and ENSO phase, and spatially, with signals varying throughout North America. Low-level zonal winds are known to have a direct impact on coastal sea levels: onshore prevailing winds (easterlies for the U.S. East Coast and westerlies for the West Coast) act to push water toward the land and raise sea level, and vice versa for offshore prevailing winds (Gill and Clarke 1974; Woodworth et al. 2019). The El Niño- associated anomaly over the North Pacific is a zonally extended westerly flow that is shifted equatorward, and westerly anomalies over Florida and the Atlantic with easterlies persisting over the Mid-Atlantic and Northeast U.S. The La Niña-associated anomaly shows a zonally contracted westerly flow shifted poleward, with weak easterly anomalies over Florida and the Atlantic, and weak westerly anomalies over the Mid-Atlantic and Northeast U.S. Both El Niño and La Niña anomalies found in Fig. 3 are reflective of the expected jet changes due to the ENSO cycle (Trenberth 1996).

As a note, we analyzed the robustness of the results from the composite maps (Figs. 3-5) by subdividing the maps into early and late boreal winter (November-January and February-April, respectively). We found that results are robust across the early and late season. Anomalies on the east and west coasts are of the same sign, with roughly equal magnitudes in the early and late season. However, there are not competing responses in the early and late seasons, and thus analyzing the teleconnection patterns across the full boreal winter (November-April) is valid.

To understand how the atmospheric variables affect the coastal sea levels on a subseasonal scale, the NTR data filtered to retain the MJO-associated anomalies for all days from 1996-2017, regardless of ENSO phase, is regressed onto the MJO-associated 850 hPa zonal wind anomalies in Fig. 6. For the regressions, a 20-day lowpass filter is applied to both the tide gauge station NTR timeseries and the 850 hPa zonal wind anomalies to remove any synoptic variability that would have been averaged out in the prior composite analyses. An additional test (not shown) was completed without applying the additional 20-day lowpass filter– the results remained qualitatively the same but the low-pass filtered anomalies had a slightly stronger magnitude due to a reduction in the variance. Thus, the "subseasonal anomalies" referred to here are a 20-120-day anomalies filtered to retain only the subseasonal signal, including that related to an MJO-forced teleconnection response. The onset of coastal impacts from these climate factors is typically only a few hours (Erikson et al. 2018), thus the variability between the subseasonal climate factors and the subseasonal tide gauge NTR anomalies can be assessed without a time lag. The same process is done for the 850 hPa meridional wind and sea level pressure anomaly regression calculations, e.g. Figure 7 shows the same NTR timseries used in Figure 6 but regressed onto the subseasonal 850 hPa meridional wind anomalies and Figure 8 shows the same NTR timseries used in Figure 6 but regressed onto the subseasonal SLP anomalies. Only regression coefficients which are significant at the 95% significance level according to a Student's two-tailed t-test are plotted. Values which are not significant are white.

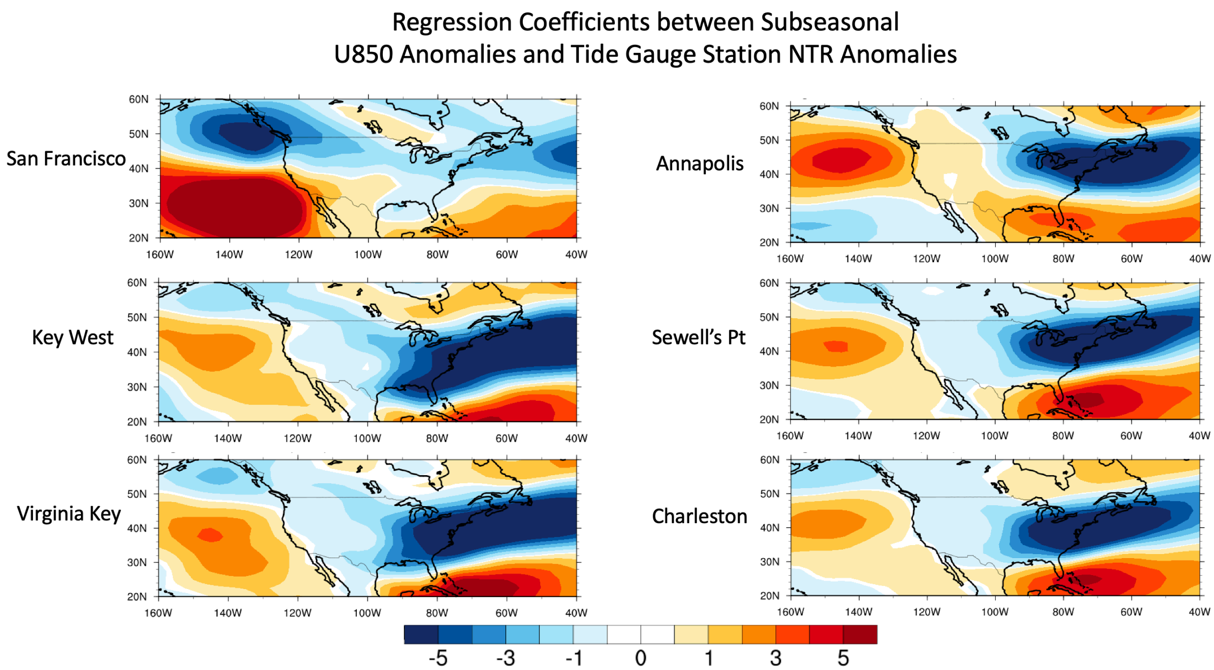

FIG. 6. Linear regression coefficients between the 20-120-day filtered subseasonal 850 hPa zonal winds (U850) and the similarly filtered subseasonal NTR anomaly timeseries for the six respective tide gauge stations for all days from 1996-2017. Only regression coefficients which are significant at the 95% significance level according to a Student's two-tailed t-test are plotted. Values which are not significant are white.

6

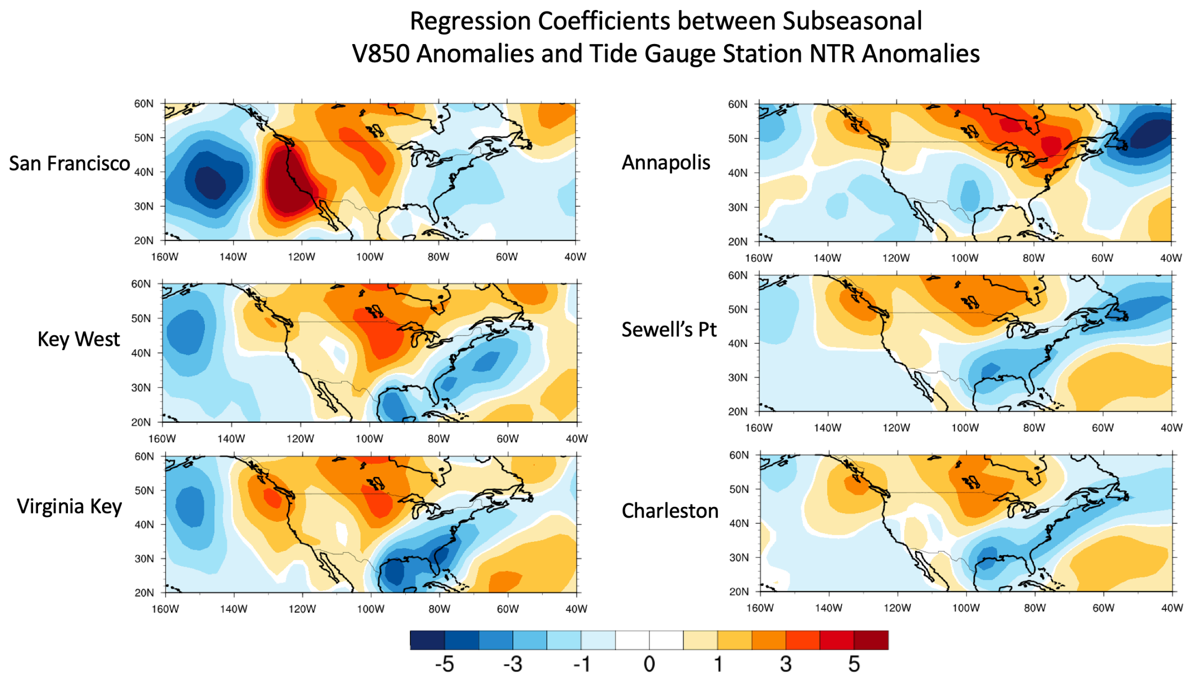

FIG. 7. Linear regression coefficients between the 20-120-day filtered subseasonal 850 hPa meridional winds (V850) and the similarly filtered subseasonal NTR anomaly timeseries for the six respective tide gauge stations for all days from 1996-2017. Only regression coefficients which are significant at the 95% significance level according to a Student's two-tailed t-test are plotted. Values which are not significant are white.

7

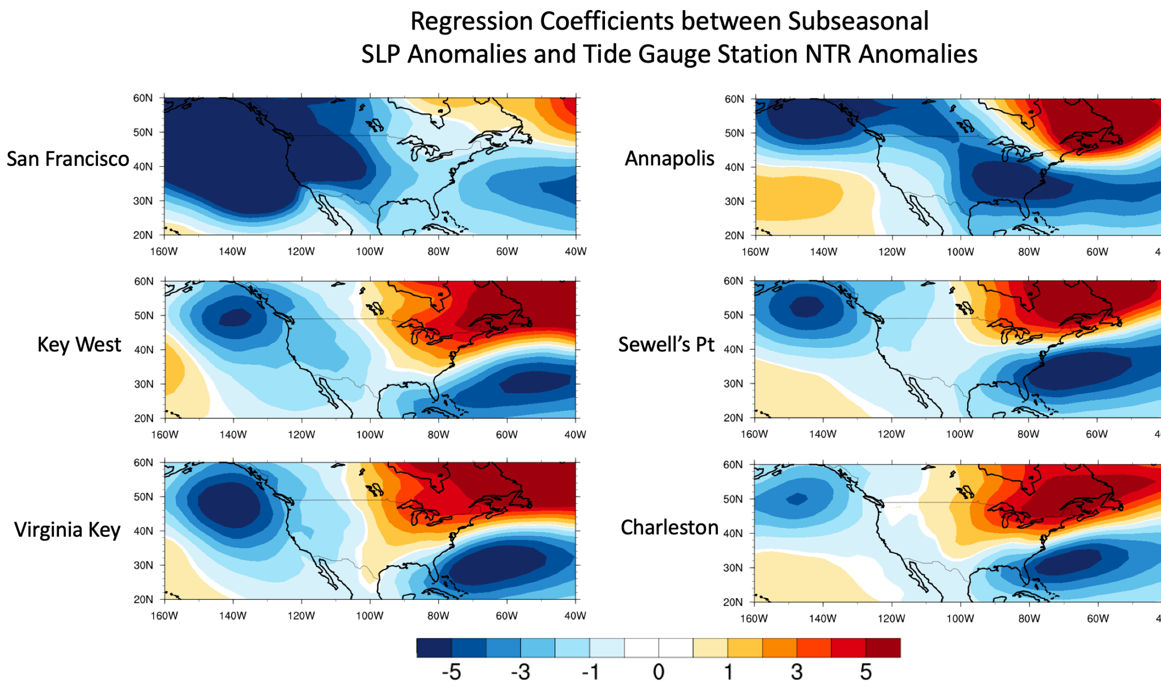

FIG. 8. Linear regression coefficients between the 20-120-day filtered subseasonal sea level pressure (SLP; hPa) and the similarly filtered subseasonal NTR anomaly timeseries for the six respective tide gauge stations for all days from 1996-2017. Only regression coefficients which are significant at the 95% significance level according to a Student's two-tailed t-test are plotted. Values which are not significant are white.

8

Figure 6 shows how the anomalous 850 hPa zonal winds potentially cause a variation in the coastal NTR sea level for each of the six tide gauge stations, due to the remote influences of the MJO. The mean flow during boreal winter consists of westerlies in the mid-latitudes and easterlies in the subtropics, creating an anticyclonic circulation at 850 hPa. At Virginia Key and Key West, there are anomalous easterlies in the mid-latitudes and anomalous westerlies in the subtropics, resulting in a weakening of the anticyclonic circulation when the NTR anomalies are higher. Thus, the anomalous cyclonic circulation at 850 hPa leads to convergence and rising motion. This also leads to reduced surface pressure, seen in Fig. 8 which shows a low pressure anomaly over Virginia Key and Key West associated with higher NTR anomalies due to the doming effect. The same holds true for the other four tide gauge stations, with the center of the anomalous cyclonic circulation and the lowest SLP centered near to the location of the tide gauge station. The sea level pressure regressions are noted to resemble the PNA-like patterns associated with MJO teleconnections documented in previous literature (Tseng et al. 2020; Seo and Lee 2017; Mori and Watanabe 2008), supporting the connection between the MJO and the response in sea level pressure, ultimately impacting sea level.

The low-level meridional wind was explored as an additional potential driver of sea level anomalies, since onshore winds at a tide gauge could be driven by zonal and/or meridional winds based on coastal location (Fig. 7). The meridional wind has highest strongest connections to San Francisco, Virginia Key, and Annapolis. Both San Francisco and and Annapolis have higher sea levels due to a southerly wind and vice versa, while Virginia Key's sea level increases due to northerly winds and vice versa.

The mechanism(s) responsible, at least in part, for sea level anomalies at the various tide gauge locations varies due to different teleconnection responses associated with both the MJO and ENSO. Furthermore, the subseasonal variability of the sea level anomalies can be linked to subseasonal variability of different atmospheric drivers based on coastal location.

c. Case Studies

The analyses thus far have examined subseasonal variability of coastal sea level anomalies over the 2-decade period from 1996-2017. We additionally investigated two specific events of coastal flooding in which the MJO and ENSO were both active to examine their potential sea level contribution to coastal flooding events.

1) Sewell's Point November 2009

In November of 2009, high water levels were reported along much of the U.S East Coast from NOAA National Ocean Services (NOS) Center for Operational Oceanographic Products and Services (CO-OPS). The highest water levels were from November 11-14 in which a Nor'easter impacted the region from Outer Banks, NC to coastal New Jersey (Egan et al. 2010). Despite the low intensity of the storm, the area, particularly Sewell's Point, endured extremely high coastal sea levels and flooding due to sustained onshore winds associated with the storm. The Virginia area (including that of Sewell's Point) was declared a major disaster after the coastal flooding event by the President of the United States (Egan et al. 2010).

During this time period, the MJO was active most of the month and there was an ongoing El Niño event. Our calculations found that the total NTR *anomaly* during the month of November 2009 at the Sewell's Point tide gauge was 191.66mm, of which 119.71mm of that occurred during MJO P23 (November 6-17) (Fig. 10a). The daily average of this anomaly during MJO P23 was 2.3x the total anomaly standard deviation (Fig. 10b). Our analysis of the low-level zonal winds and sea level pressure (Fig. 10c-d) revealed persistent easterly winds during MJO P23, consistent with the report by Egan et al. (2010). Further, previous studies have shown that during El Niños, coastal winter storm tracks and prevailing winds lead to more extratropical winter storms on average which impact the East Coast (Hirsch et al. 2001; Sweet and Zervas 2011; Thompson et al. 2013), as was seen in November of 2009. The results show the El Niño-associated low frequency anomaly was weak westerlies, consistent with the expected El Niño zonal wind response (Fig. 3b), but easterly winds were associated with the subseasonal MJO signal. The sea level pressure anomalies associated with both the MJO and El Niño are weak over the Sewell's Point area, and thus did not likely play a role in the coastal flooding mechanisms. Thus, the combination of an active MJO and El Niño contributed to an environment which was conducive for extratropical storm formation leading to prevailing onshore winds and higher sea levels. Further, a subseasonal signal from the MJO helped set up an environment which contributed to the historic high water levels in Sewell's Point in November of 2009.

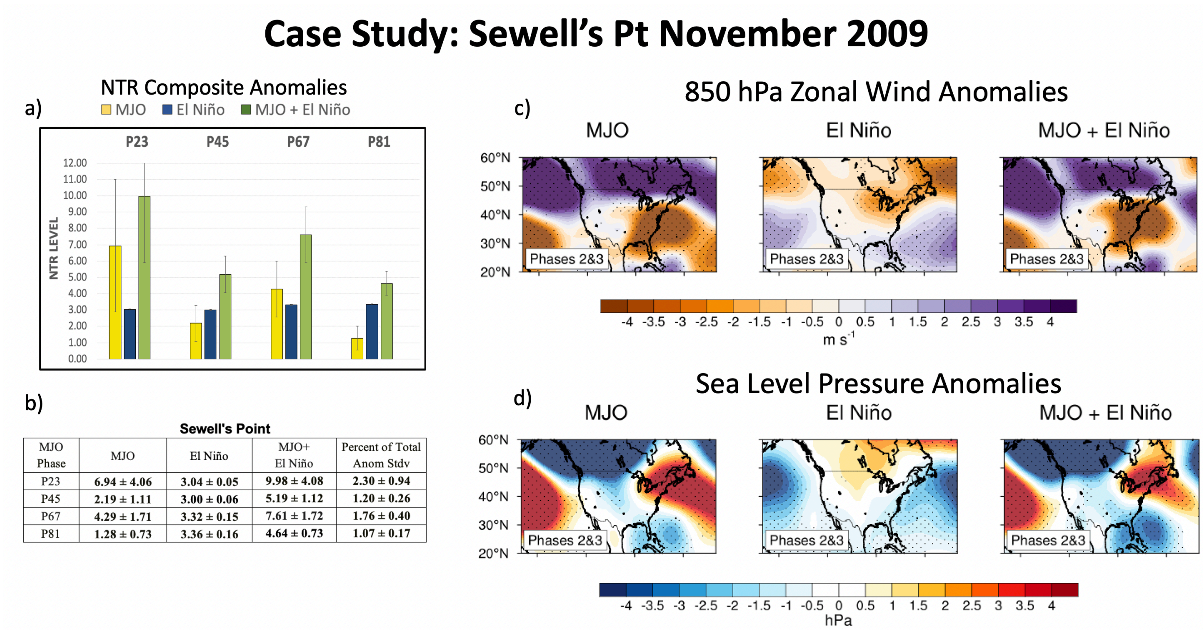

MJO Phase	MJO	El Niño	MJO+ El Niño	Percent of Total Anom Stdv
P23	6.94 ± 4.06	3.04 ± 0.05	9.98 ± 4.08	2.30 ± 0.94
P45	2.19 ± 1.11	3.00 ± 0.06	5.19 ± 1.12	1.20 ± 0.26
P67	4.29 ± 1.71	3.32 ± 0.15	7.61 ± 1.72	1.76 ± 0.40
P81	1.28 ± 0.73	3.36 ± 0.16	4.64 ± 0.73	1.07 ± 0.17

FIG. 9. Analyses for a case study at Sewell's Point for November 2009. a) NTR anomalies in millimeters broken down by MJO phase (P23, P45, P67, P81) for active MJO days in November 2009. The yellow bars show MJO-only anomalies, the blue bars show the ENSO-only anomalies, and the green bars are the MJO+ENSO anomalies. The error bars show plus/minus one standard deviation of 10,000 bootstrapped samples. b) Numeric values of the bar charts in a). The rightmost column shows the percentage of the combined MJO+ENSO anomaly to the total anomaly standard deviation. Values include plus/minus one standard deviation computed via 10,000 iterations of bootstrapping. MJO phases in which constructive interference occurred are bolded. c) 850 hPa Zonal wind Anomalies similarly composited but just for MJO P23. Stippling indicates anomalies which exceed two standard deviations. d) Same as c) but for sea level pressure anomalies in hPa. MJO P23 is Nov 6-17, P45 is Nov 18-21, P67 is Nov 26-28, and P81 is Nov 1-5 for a total of 25 days used.

2) Key West November 2016

In November of 2016 in Key West, the National Weather Service issued a Coastal Flood Statement declaring that the Key West tide gauge had crossed the threshold of 1.1ft (0.335m) above the mean higher high water level (`https://www.weather.gov/key/coastal_flooding#WaterLevels`). These statements have only been issued 39 months out of the 480 months on record. Notably, this statement was issued during an ongoing La Niña event, which is shown in Figure 2 to reduce sea level heights in Key West.

We analyzed the contributions of both the MJO and ENSO-associated anomalies to this event. We found that the largest anomalies occurred during P67 and P81, with a cumulative 26.57mm associated with the MJO+ENSO combined anomaly (Fig. 2a-b). The majority of this contribution, 22.69mm, was associated with the MJO. This MJO contribution to the NTR anomaly during this time is notable, because not only was the La Niña anomaly slightly positive despite the typical La Niña anomaly in this region being negative, but also the MJO-associated anomaly was an order of magnitude higher than the average MJO-associated anomaly during P67 and P81 (Table 2). Thus, a combination of a slightly positive La Niña anomaly and constructive interference with a large positive MJO anomaly contributed to the flooding event during that time.

Analysis of the atmospheric variables shows destructive interference during P81 (e.g. the highest sea level anomaly period) of MJO-associated westerly winds and La Niña- associated easterly winds (Fig. 2c-d). Further, the SLP anomaly was a low associated with the MJO and insignificant contribution from the La Niña signal. Therefore, it is suggested that the MJO teleconnection response led to a low sea level pressure anomaly over the Key West region, resulting in a doming effect and increased sea levels, which helped contribute to the high water levels in Key West in November of 2016.

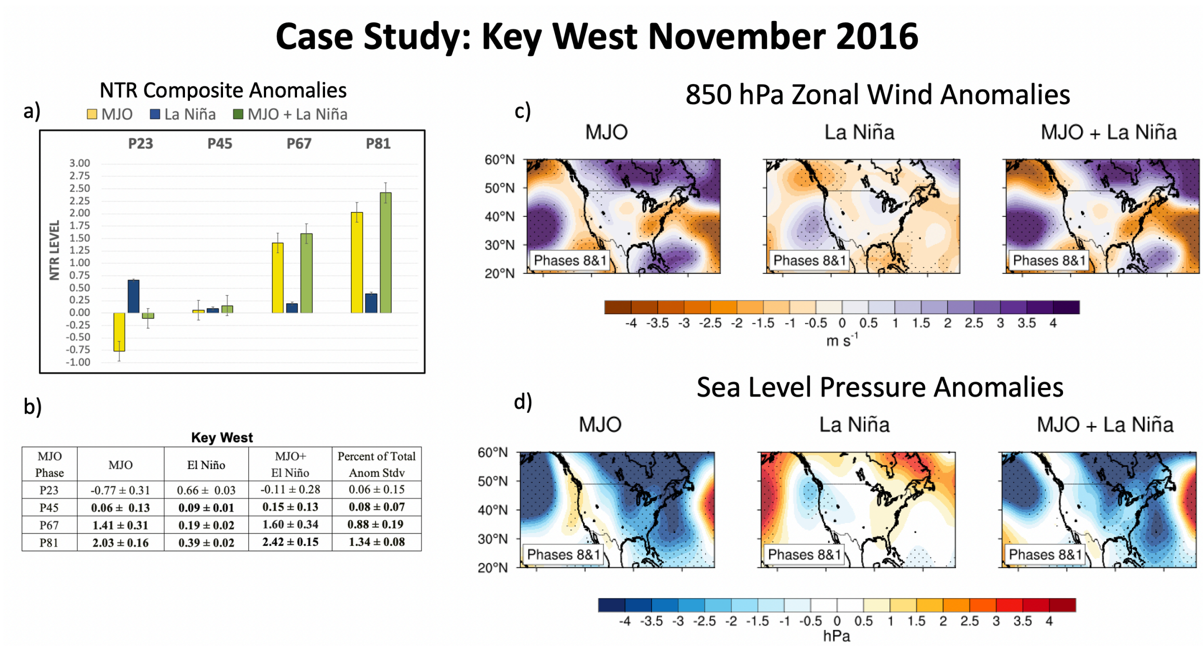

MJO Phase	MJO	El Niño	MJO+ El Niño	Percent of Total Anom Stdv
P23	-0.77 ± 0.31	0.66 ± 0.03	-0.11 ± 0.28	0.06 ± 0.15
P45	**0.06 ± 0.13**	**0.09 ± 0.01**	**0.15 ± 0.13**	**0.08 ± 0.07**
P67	**1.41 ± 0.31**	**0.19 ± 0.02**	**1.60 ± 0.34**	**0.88 ± 0.19**
P81	**2.03 ± 0.16**	**0.39 ± 0.02**	**2.42 ± 0.15**	**1.34 ± 0.08**

FIG. 10. Analyses for a case study at Key West for November 2016. a) NTR anomalies in millimeters broken down by MJO phase (P23, P45, P67, P81) for active MJO days in November 2016. The yellow bars show MJO-only anomalies, the blue bars show the ENSO-only anomalies, and the green bars are the MJO+ENSO anomalies. The error bars show plus/minus one standard deviation of 10,000 bootstrapped samples. b) Numeric values of the bar charts in a). The rightmost column shows the percentage of the combined MJO+ENSO anomaly to the total anomaly standard deviation. Values include plus/minus one standard deviation computed via 10,000 iterations of bootstrapping. MJO phases in which constructive interference occurred are bolded. c) 850 hPa Zonal wind Anomalies similarly composited but just for MJO P23. Stippling indicates anomalies which exceed two standard deviations. d) Same as c) but for sea level pressure anomalies in hPa. MJO P23 is Nov 19-24,26, P45 is Nov 4-5, P67 is Nov 6-11, and P81 is Nov 12-18 for a total of 22 days used.

10

4. Conclusions and Discussion

MJO deep convection triggers a tropical-extratropical teleconnection response via poleward-propagating stationary Rossby waves that can be found in the U.S. coastal sea levels. We find that during particular phases of the MJO, the ENSO-associated non-tidal residual (NTR) coastal sea level anomaly can be significantly enhanced or masked by the MJO-associated anomaly, consistent with findings of Arcodia et al. (2020) documenting MJO and ENSO interference in U.S. rainfall and geopotential height patterns.

On the East Coast of the U.S., the NTR anomaly associated with the MJO destructively interferes with the positive anomaly associated with El Niño and constructively interferes with the La Niña anomaly during MJO P23 and P45. During P81, the opposite occurs in which the MJO and ENSO signals constructively interfere during El Niño and destructively interfere during La Niña, revealing subseasonal variability in NTR anomalies due to the MJO and interference with ENSO. P67 show more case-by-case variability. Discrepancies in the MJO-associated anomalies during El Niño and La Niña strengthen the argument that ENSO is modulated by the MJO teleconnection pattern over North America.

On the West Coast, the NTR anomaly is dominated by the ENSO signal. Despite some constructive and destructive interference from the MJO, the combined anomaly is due primarily to the ENSO anomaly. This is consistent with previous work showing that ENSO can contribute significantly to sea level change along the West Coast of the U.S. (Hamlington et al. 2015) due to higher sea levels from warmer ocean temperatures and deeper thermoclines (Enfield and Allen 1980; Chelton and Davis 1982; Goodman et al. 2018), while the East Coast sea level is impacted by ENSO via atmospheric teleconnections.

A possible mechanism is proposed for how the MJO and ENSO remote forcings can impact U.S. coastal NTR levels. Composite analysis of MJO- and ENSO- associated 850 hPa zonal wind and SLP reveals that SLP anomalies are a better indicator of coastal NTR anomalies in South Florida than low-level zonal winds anomalies. Both the low-level zonal winds and the SLP are good indicators of coastal NTR anomalies at Sewell's Point and Charleston, with stronger signals during El Niños than La Niñas. On the West Coast, the NTR anomaly is primarily a direct response to ENSO with little influence from the MJO. Additionally, an anomalous 850 hPa cyclonic circulation over the tide gauge location forced by the MJO deep convection weakens the anticyclonic mean flow leading to a surface low and resultant positive NTR anomalies at the tide gauge location. Anomalous 850 hPa meridional winds are connected to increases in sea level in San Francisco, Virginia Key, and Annapolis. We note that there is a distinction between the factors that affect large-scale ocean circulation and coastal level changes. However, numerous studies have explored links between the physical mechanisms of large-scale forcing factors (including but not limited to internal variability as investigated here) and coastal sea level changes (Woodworth et al. 2019; Piecuch et al. 2019; Durand et al. 2019; Ponte et al. 2019, 2020), but more research in this area will help strengthen our understanding of this relationship.

Two case studies were examined to link the broader scale remote influences on U.S. coastal sea level to observed high-impact flooding events. We found that during November of 2019, constructive interference of MJO and El Niño signals contributed to the extremely high sea levels, particularly due to persistent onshore winds. Additionally, in November of 2016, we found that a positive La Niña sea level anomaly (opposite sign than expected) constructively interefered with the large MJO sea level anomaly, contributing to the coastal flooding observed during that month.

This analysis reveals that the MJO is playing a role in anomalous NTR water levels and moreover, the MJO signal constructively and destructively interferes with the ENSO signal which impacts the anomalous NTR levels. It is noted that additional factors are likely at play in coastal water levels, spanning temporal and spatial scales. Hamlington et al. (2015) found a connection between the Pacific Decadal Oscillation and East and West Coast water levels. Shorter scale influences, such as dynamical effects of wind waves and storm surge, in combination with subseasonal and longer temporal scales should be considered, along with regional and local influences for a holistic understanding of coastal water level variations. Further, the role of the Gulf Stream and the Florida Current is known to play a role in East Coast flooding and potentially accelerated flooding in some areas (Ezer et al. 2013; Ezer and Atkinson 2014) and also merits further attention. The influence of the location of the tide gauges should also be further explored, as not all tide gauges are located in similar coastal regions (i.e. the Virginia Key tide gauge is located on Biscayne Bay while the Sewell's Point tide gauge is located at the mouth of the James River). Of critical importance, the impacts and consequences of subseasonal to seasonal climate variability on sea level will amplify as certain climate modes can accelerate or decelerate the sea level trend. Understanding the role of subseasonal variability on coastal water levels will contribute to more precise regionalized flooding projections and aid in more effective mitigation, adaptation, and future planning efforts.

Acknowledgments. M.A. acknowledges the support from NOAA NA18OAR4310293, NA20OAR4320472. B.K. and E.B. acknowledge the support from NOAA (NA18OAR4310293, NA15OAR4320064, NA20OAR4320472), NSF (OCE1419569, OCE1559151), and DOE (DE-SC0019433). B.K. is the William R Middelthon Chair of Earth Sciences and is grateful for the associated support. The authors wish to thank Brian Mapes and Breanna Zavadoff for helpful insights for this research and Richard Karp for assistance with data visualization.

Data availability statement. The NCEP-NCAR Reanalysis-2 data can be accessed online at https://psl.noaa.gov/data/gridded/data.ncep.Reanalysis2.html. The water level data used for calculating the non-tidal residual is available from the Center for Operational Oceanographic Products and Services (CO-OPS) (http://tidesandcurrents.noaa.gov/).

References

Alexander, M. A., I. Bladé, M. Newman, J. R. Lanzante, N.-C. Lau, and J. D. Scott, 2002: The atmospheric bridge: The influence of enso teleconnections on air–sea interaction over the global oceans. *Journal of Climate*, **15 (16)**, 2205–2231.

Andrews, E., R. C. Antweiler, P. J. Neiman, and F. M. Ralph, 2004: Influence of enso on flood frequency along the california coast. *Journal of Climate*, **17 (2)**, 337–348.

Arcodia, M. C., and B. P. Kirtman, 2023: Using simplified linear and nonlinear models to assess enso-modulated mjo teleconnections. *Climate Dynamics*, 1–21.

Arcodia, M. C., B. P. Kirtman, and L. S. Siqueira, 2020: How mjo teleconnections and enso interference impacts us precipitation. *Journal of Climate*, **33 (11)**, 4621–4640.

Barnard, P. L., and Coauthors, 2015: Coastal vulnerability across the pacific dominated by el nino/southern oscillation. *Nature Geoscience*, **8 (10)**, 801–807.

Becker, E. J., E. H. Berbery, and R. W. Higgins, 2011: Modulation of cold-season us daily precipitation by the madden–julian oscillation. *Journal of Climate*, **24 (19)**, 5157–5166.

Buchanan, M. K., S. Kulp, L. Cushing, R. Morello-Frosch, T. Nedwick, and B. Strauss, 2020: Sea level rise and coastal flooding threaten affordable housing. *Environmental Research Letters*, **15 (12)**, 124 020.

Chapman, W. E., A. C. Subramanian, S.-P. Xie, M. D. Sierks, F. M. Ralph, and Y. Kamae, 2021: Monthly modulations of enso teleconnections: Implications for potential predictability in north america. *Journal of Climate*, **34 (14)**, 5899–5921.

Chelton, D. B., and R. E. Davis, 1982: Monthly mean sea-level variability along the west coast of north america. *Journal of Physical Oceanography*, **12 (8)**, 757–784.

Church, J. A., and N. J. White, 2011: Sea-level rise from the late 19th to the early 21st century. *Surveys in Geophysics*, **32 (4)**, 585–602.

Compo, G. P., P. D. Sardeshmukh, and C. Penland, 2001: Changes of subseasonal variability associated with el niño. *Journal of climate*, **14 (16)**, 3356–3374.

Dasgupta, S., B. Laplante, S. Murray, and D. Wheeler, 2009: Sea-level rise and storm surges: A comparative analysis of impacts in developing countries. *World Bank Policy Research Working Paper*, **(4901)**.

Diaz, H. F., M. P. Hoerling, and J. K. Eischeid, 2001: Enso variability, teleconnections and climate change. *International Journal of Climatology*, **21 (15)**, 1845–1862.

Durand, F., C. G. Piecuch, M. Becker, F. Papa, S. V. Raju, J. U. Khan, and R. M. Ponte, 2019: Impact of continental freshwater runoff on coastal sea level. *Surveys in Geophysics*, **40**, 1437–1466.

Egan, K., L. Brown, K. L. Earwaker, A. Grodsky, and Z. Aijun, 2010: Effects of the november 2009 nor'easter on water levels.

Enfield, D. B., and J. Allen, 1980: On the structure and dynamics of monthly mean sea level anomalies along the pacific coast of north and south america. *Journal of Physical Oceanography*, **10 (4)**, 557–578.

Enríquez, A. R., T. Wahl, H. E. Baranes, S. A. Talke, P. M. Orton, J. F. Booth, and I. D. Haigh, 2022: Predictable changes in extreme sea levels and coastal flood risk due to long-term tidal cycles. *Journal of Geophysical Research: Oceans*, **127 (4)**, e2021JC018 157.

Erikson, L. H., and Coauthors, 2018: Identification of storm events and contiguous coastal sections for deterministic modeling of extreme coastal flood events in response to climate change. *Coastal Engineering*, **140**, 316–330.

Ezer, T., 2019: Regional differences in sea level rise between the mid-atlantic bight and the south atlantic bight: Is the gulf stream to blame? *Earth's Future*, **7 (7)**, 771–783.

Ezer, T., and L. P. Atkinson, 2014: Accelerated flooding along the us east coast: On the impact of sea-level rise, tides, storms, the gulf stream, and the north atlantic oscillations. *Earth's Future*, **2 (8)**, 362–382.

Ezer, T., L. P. Atkinson, W. B. Corlett, and J. L. Blanco, 2013: Gulf stream's induced sea level rise and variability along the us mid-atlantic coast. *Journal of Geophysical Research: Oceans*, **118 (2)**, 685–697.

Gill, A., and A. Clarke, 1974: Wind-induced upwelling, coastal currents and sea-level changes. *Deep Sea Research and Oceanographic Abstracts*, Elsevier, Vol. 21, 325–345.

Goodman, A. C., K. M. Thorne, K. J. Buffington, C. M. Freeman, and C. N. Janousek, 2018: El niño increases high-tide flooding in tidal wetlands along the us pacific coast. *Journal of Geophysical Research: Biogeosciences*, **123 (10)**, 3162–3177.

Griggs, G., 2021: Rising seas in california—an update on sea-level rise science. *World Scientific Encyclopedia of Climate Change: Case Studies of Climate Risk, Action, and Opportunity Volume 3*, World Scientific, 105–111.

Hamlington, B., R. Leben, K.-Y. Kim, R. Nerem, L. Atkinson, and P. Thompson, 2015: The effect of the el niño-southern oscillation on us regional and coastal sea level. *Journal of Geophysical Research: Oceans*, **120 (6)**, 3970–3986.

Held, I. M., and I.-S. Kang, 1987: Barotropic models of the extratropical response to el niflo. *Journal of Atmospheric Sciences*, **44 (23)**, 3576–3586.

Henderson, S. A., E. D. Maloney, and E. A. Barnes, 2016: The influence of the madden–julian oscillation on northern hemisphere winter blocking. *Journal of Climate*, **29 (12)**, 4597–4616.

Henderson, S. A., E. D. Maloney, and S.-W. Son, 2017: Madden–julian oscillation pacific teleconnections: The impact of the basic state and mjo representation in general circulation models. *Journal of Climate*, **30 (12)**, 4567–4587.

Hino, M., S. T. Belanger, C. B. Field, A. R. Davies, and K. J. Mach, 2019: High-tide flooding disrupts local economic activity. *Science advances*, **5 (2)**, eaau2736.

Hirsch, M. E., A. T. DeGaetano, and S. J. Colucci, 2001: An east coast winter storm climatology. *Journal of Climate*, **14 (5)**, 882–899.

Hoskins, B. J., and D. J. Karoly, 1981: The steady linear response of a spherical atmosphere to thermal and orographic forcing. *Journal of the Atmospheric Sciences*, **38 (6)**, 1179–1196.

IPCC, 2022: Climate change 2022: Impacts, adaptation, and vulnerability. contribution of working group ii to the sixth assessment report of the intergovernmental panel on climate change [h.-o. pörtner, d.c. roberts, m. tignor, e.s. poloczanska, k. mintenbeck, a. alegría, m. craig, s. langsdorf, s. löschke, v. möller, a. okem, b. rama (eds.)]. cambridge university press. cambridge university press, cambridge, uk and new york, ny, usa, 3056 pp., doi:10.1017/9781009325844.

Jenney, A., K. Nardi, E. Barnes, and D. Randall, 2019: The seasonality and regionality of mjo impacts on north american temperature. *Geophysical Research Letters*, **46 (15)**, 9193–9202.

Kalnay, E., and Coauthors, 1996: The ncep/ncar 40-year reanalysis project. *Bulletin of the American Meteorological Society*, **77 (3)**, 437–472.

Li, S., and Coauthors, 2022: Contributions of different sea-level processes to high-tide flooding along the us coastline. *Journal of Geophysical Research: Oceans*, **127 (7)**, e2021JC018 276.

Lin, H., G. Brunet, and J. Derome, 2008: Forecast skill of the madden–julian oscillation in two canadian atmospheric models. *Monthly Weather Review*, **136 (11)**, 4130–4149.

Long, X., and Coauthors, 2021: Seasonal forecasting skill of sea-level anomalies in a multi-model prediction framework. *Journal of Geophysical Research: Oceans*, **126 (6)**, e2020JC017 060.

Madden, R. A., and P. R. Julian, 1971: Detection of a 40–50 day oscillation in the zonal wind in the tropical pacific. *Journal of the Atmospheric Sciences*, **28 (5)**, 702–708.

Madden, R. A., and P. R. Julian, 1972: Description of global-scale circulation cells in the tropics with a 40–50 day period. *Journal of the Atmospheric Sciences*, **29 (6)**, 1109–1123.

Marcos, M., F. M. Calafat, Á. Berihuete, and S. Dangendorf, 2015: Long-term variations in global sea level extremes. *Journal of Geophysical Research: Oceans*, **120 (12)**, 8115–8134.

Marcos, M., and P. L. Woodworth, 2017: Spatiotemporal changes in extreme sea levels along the coasts of the n orth a tlantic and the g ulf of m exico. *Journal of Geophysical Research: Oceans*, **122 (9)**, 7031–7048.

Mariotti, A., and Coauthors, 2020: Windows of opportunity for skillful forecasts subseasonal to seasonal and beyond. *Bulletin of the American Meteorological Society*, **101 (5)**, E608–E625.

Martello, M. V., and A. J. Whittle, 2023: Estimating coastal flood damage costs to transit infrastructure under future sea level rise. *Communications Earth & Environment*, **4 (1)**, 137.

Matthews, A. J., B. J. Hoskins, and M. Masutani, 2004: The global response to tropical heating in the madden–julian oscillation during the northern winter. *Quarterly Journal of the Royal Meteorological Society: A Journal of the Atmospheric Sciences, Applied Meteorology and Physical Oceanography*, **130 (601)**, 1991–2011.

Menéndez, M., and P. L. Woodworth, 2010: Changes in extreme high water levels based on a quasi-global tide-gauge data set. *Journal of Geophysical Research: Oceans*, **115 (C10)**.

Merrifield, M. A., A. S. Genz, C. P. Kontoes, and J. J. Marra, 2013: Annual maximum water levels from tide gauges: Contributing factors and geographic patterns. *Journal of Geophysical Research: Oceans*, **118 (5)**, 2535–2546.

Moon, J.-Y., B. Wang, and K.-J. Ha, 2011: Enso regulation of mjo teleconnection. *Climate Dynamics*, **37 (5-6)**, 1133–1149.

Mori, M., and M. Watanabe, 2008: The growth and triggering mechanisms of the pna: A mjo-pna coherence. *Journal of the Meteorological Society of Japan. Ser. II*, **86 (1)**, 213–236.

Muis, S., I. D. Haigh, G. Guimarães Nobre, J. C. Aerts, and P. J. Ward, 2018: Influence of el niño-southern oscillation on global coastal flooding. *Earth's Future*, **6 (9)**, 1311–1322.

Nicholls, R. J., and Coauthors, 2021: A global analysis of subsidence, relative sea-level change and coastal flood exposure. *Nature Climate Change*, **11 (4)**, 338–342.

Oliver, E., and K. Thompson, 2010: Madden-julian oscillation and sea level: Local and remote forcing. *Journal of Geophysical Research: Oceans*, **115 (C1)**.

Piecuch, C., F. Calafat, S. Dangendorf, and G. Jordà, 2019: The ability of barotropic models to simulate historical mean sea level changes from coastal tide gauge data. *Surveys in geophysics*, **40**, 1399–1435.

Ponte, R. M., B. Meyssignac, C. M. Domingues, D. Stammer, A. Cazenave, and T. Lopez, 2019: Guest editorial: relationships between coastal sea level and large-scale ocean circulation. *Surveys in Geophysics*, **40**, 1245–1249.

Ponte, R. M., B. Meyssignac, C. M. Domingues, D. Stammer, A. Cazenave, and T. Lopez, 2020: *Relationships Between Coastal Sea Level and Large Scale Ocean Circulation*. Springer.

Ren, H.-L., Y. Wei, and S. Zhao, 2022: Low-frequency variability in the real-time multivariate mjo index: Real or artificial? *Journal of Climate*, 1–33.

Roundy, P., 2012: Tropical-extratropical interactions. intraseasonal variability of the atmosphere–ocean climate system, wk-m. lau and de waliser, eds. Springer.

Ryan, H., and M. Noble, 2002: Sea level response to enso along the central california coast: how the 1997–1998 event compares with the historic record. *Progress in Oceanography*, **54 (1-4)**, 149–169.

Seo, K.-H., and H.-J. Lee, 2017: Mechanisms for a pna-like teleconnection pattern in response to the mjo. *Journal of the Atmospheric Sciences*, **74 (6)**, 1767–1781.

Stan, C., D. M. Straus, J. S. Frederiksen, H. Lin, E. D. Maloney, and C. Schumacher, 2017: Review of tropical-extratropical teleconnections on intraseasonal time scales. *Reviews of Geophysics*, **55 (4)**, 902–937.

Swain, D., O. E. Wing, P. D. Bates, J. Done, K. Johnson, and D. Cameron, 2020: Increased flood exposure due to climate change and population growth in the united states. *Earth's Future*, **8 (11)**, e2020EF001 778.

Sweet, W., G. Dusek, D. C. Marcy, G. Carbin, and J. Marra, 2019: 2018 state of us high tide flooding with a 2019 outlook.

Sweet, W. V., and J. Park, 2014: From the extreme to the mean: Acceleration and tipping points of coastal inundation from sea level rise. *Earth's Future*, **2 (12)**, 579–600.

Sweet, W. V., J. Park, S. Gill, and J. Marra, 2015: New ways to measure waves and their effects at noaa tide gauges: A hawaiian-network perspective. *Geophysical Research Letters*, **42 (21)**, 9355–9361.

Sweet, W. V., and C. Zervas, 2011: Cool-season sea level anomalies and storm surges along the us east coast: Climatology and comparison with the 2009/10 el niño. *Monthly Weather Review*, **139 (7)**, 2290–2299.

Sweet, W. V., William, G. Dusek, J. Obeysekera, and J. J. Marra, 2018: Patterns and projections of high tide flooding along the us coastline using a common impact threshold. *NOAA Technical Report*.

Sweet, W. W. V., R. Kopp, C. P. Weaver, J. Obeysekera, R. M. Horton, E. R. Thieler, C. E. Zervas, and Coauthors, 2017: Global and regional sea level rise scenarios for the united states. *NOAA Technical Report*.

Taschetto, A. S., C. C. Ummenhofer, M. F. Stuecker, D. Dommenget, K. Ashok, R. R. Rodrigues, and S.-W. Yeh, 2020: Enso atmospheric teleconnections. *El Niño southern oscillation in a changing climate*, 309–335.

Thompson, P. R., G. T. Mitchum, C. Vonesch, and J. Li, 2013: Variability of winter storminess in the eastern united states during the twentieth century from tide gauges. *Journal of Climate*, **26 (23)**, 9713–9726.

Tibshirani, R. J., and B. Efron, 1993: An introduction to the bootstrap. *Monographs on statistics and applied probability*, **57 (1)**.

Trenberth, K. E., 1996: El niño southern oscillation (enso). *Sea*.

Tseng, K.-C., E. Maloney, and E. Barnes, 2019: The consistency of mjo teleconnection patterns: An explanation using linear rossby wave theory. *Journal of Climate*, **32 (2)**, 531–548.

Tseng, K.-C., E. Maloney, and E. A. Barnes, 2020: The consistency of mjo teleconnection patterns on interannual time scales. *Journal of Climate*, **33 (9)**, 3471–3486.

Vitart, F., and Coauthors, 2017: The subseasonal to seasonal (s2s) prediction project database. *Bulletin of the American Meteorological Society*, **98 (1)**, 163–173.

Vitart, F., and Coauthors, 2019: Sub-seasonal to seasonal prediction of weather extremes. *Sub-seasonal to seasonal prediction*, Elsevier, 365–386.

Warren-Myers, G., and A. Hurlimann, 2022: Climate change and risk to real estate. *A Research Agenda for Real Estate*, Edward Elgar Publishing.

Wheeler, M. C., and H. H. Hendon, 2004: An all-season real-time multivariate mjo index: Development of an index for monitoring and prediction. *Monthly Weather Review*, **132 (8)**, 1917–1932.

Woodworth, P. L., and Coauthors, 2019: Forcing factors affecting sea level changes at the coast. *Surveys in Geophysics*, **40 (6)**, 1351–1397.

Yadav, P., and D. M. Straus, 2017: Circulation response to fast and slow mjo episodes. *Monthly Weather Review*, **145 (5)**, 1577–1596.

Yeh, S.-W., and Coauthors, 2018: Enso atmospheric teleconnections and their response to greenhouse gas forcing. *Reviews of Geophysics*, **56 (1)**, 185–206.

Zhang, C., 2005: Madden-julian oscillation. *Reviews of Geophysics*, **43 (2)**.

Zhang, C., 2013: Madden–julian oscillation: Bridging weather and climate. *Bulletin of the American Meteorological Society*, **94 (12)**, 1849–1870.

Zheng, C., and E. Chang, 2019: The role of mjo propagation, lifetime, and intensity on modulating the temporal evolution of the mjo extratropical response. *Journal of Geophysical Research: Atmospheres*, **124 (10)**, 5352–5378.